Biosensors and Bioelectronics 42 (2013) 550–555

Contents lists available at SciVerse ScienceDirect

Biosensors and Bioelectronics

journal homepage: www.elsevier.com/locate/bios

Highly sensitive detection of hydrogen peroxide based on nanoporous Fe_2O_3/CoO composites

Jinping Wang [a], Hua Gao [b], Fenglei Sun [b], Qin Hao [a], Caixia Xu [a,*]

[a] Key Laboratory of Chemical Sensing & Analysis in Universities of Shandong, School of Chemistry and Chemical Engineering, University of Jinan, Jinan 250022, China
[b] Affiliated Hospital of Shandong University of Traditional Chinese Medicine, Jinan 250011, China

ARTICLE INFO

Article history:
Received 28 September 2012
Received in revised form
8 November 2012
Accepted 12 November 2012
Available online 24 November 2012

Keywords:
Metal oxides
Fe_2O_3/CoO composites
Electro-oxidation
Hydrogen peroxide
Dealloying
Biosensing

ABSTRACT

Nanoporous (NP) Fe_2O_3/CoO composites were straightforwardly fabricated by a simple dealloying strategy. Electron microscopy characterization demonstrates that selectively etching FeCoAl ternary alloy in a low concentration of NaOH solution generates a nanoparticle structure with a typical diameter around 80 nm. Interestingly, these nanoparticles consist of open three-dimensional bicontinuous nanosponge structure with uniform pore and ligament distribution around 10 nm. The resulted sample is confirmed to be a mixture of Fe_2O_3 and CoO species based on X-ray photoelectron spectroscopy and X-Ray diffraction analysis. Without any activation pretreatment, NP-Fe_2O_3/CoO composites exhibit excellent electro-oxidation activity toward H_2O_2, such as an excellent sensing performance in a wide linear sensing region from 0.05 to 4.85 mM H_2O_2, fast amperometric response (<2 s), and a lower detection limit to 0.1 μM. Along with these attractive features, the as-made composites also behave as a good anti-interference towards glucose, uric acid, dopamine, and ascorbic acid during H_2O_2 detection. Furthermore, the H_2O_2 biosensor based on NP-Fe_2O_3/CoO composites also exhibits excellent long-term stability and reproducibility.

1. Introduction

The dealloying method has demonstrated to be a powerful and versatile strategy to fabricate nanoporous metallic materials, in which selective etching of the source alloy leaves behind the desired elements self-assembling to form a three-dimensional sponge-like porous structure (Xu et al., 2011; Chen et al., 2011; Erlebacher et al., 2001; Cattarin1 et al., 2009). For example, a variety of nanoporous metals, such as PtCo, PtCu, PtFe, PtAu alloys have been synthesized through electrochemical or chemical dealloying of appropriate source alloys (Lai et al., 2010; Koh and Strasser, 2007; Xu et al., 2009, 2012; Snyder et al., 2008; Highfield et al., 2009; Lang et al., 2010; Yu et al., 2008). However, it is much less appreciated that this simple dealloying approach can be extended to fabricate important transition metal oxide nanomaterials. For instance, Xu et al. (2010) successfully synthesized several metal oxide nanostructures by an unusually simple yet highly effective alloy corrosion method, such as Co_3O_4 nanosheets, Fe_3O_4 and Mn_3O_4 nanooctahedron by dealloying corresponding Al-based source alloys. Qi et al. (2011) prepared nanoporous Cu/ $(FeCu)_3O_4$ oxides by one-step dealloying. During the dealloying process, the main mechanism for the formation of metal oxides is because the target metals are more reactive, which undergoes spontaneous oxidation and grows into different morphologies by combining with oxygen in electrolyte or air during the dealloying and drying procedure. By carefully selecting source alloy compositions and etching conditions, this method can in principle offer very flexible control to various metal oxides. Considering these interesting findings, it is intriguing to explore the structural evolution and formation when dealloying ternary source alloy containing two more reactive metals, such as dealloying of FeCoAl alloys. In current work, we explore the structure formation and evolution by etching FeCoAl source alloy with equal content of Fe and Co and investigate the sensing performance of the resulted sample towards H_2O_2.

As an efficient liquid oxidant, H_2O_2 has wide applications in environmental, pharmaceutical, clinical, and industrial research. Furthermore, H_2O_2 is an essential mediator or a common by-product involved in many chemical and biological processes (Meng et al., 2011). Consequently, in recent years H_2O_2 has attracted enormous attention due to its significant importance in the fields of food, clinical and enzymatic related reactions etc (Chen et al., 2012a, 2012b). In previous reports, metallic nanomaterials, such as Pt, Au, PtPd etc. are currently the most investigated for H_2O_2 sensing because of their excellent electrocatalytic activity (Bo et al., 2011; Chakraborty and Raj, 2009; Niu et al., 2012; Kong et al., 2010; You et al., 2011). However, these metals are precious, which are not desired considering as the

* Corresponding author. Tel.: +86 0531 82767367.
E-mail address: chm_xucx@ujn.edu.cn (C. Xu).

0956-5663/$ - see front matter © 2012 Elsevier B.V. All rights reserved.
http://dx.doi.org/10.1016/j.bios.2012.11.016

higher catalyst cost. Additionally, it is essential to further enhance the direct electron transfer rate in the H_2O_2 biosensor for increasing the sensitivity and improving the response time. Therefore, non-precious transition metals and their oxides have attracted more and more attention in recent study (Chen et al., 2012b). In previous reports, transition metal oxides have been used in amino acid biosensor, glucose sensing, H_2O_2 biosensor and cell monitoring due to their surface redox reactivity properties (Nambiar et al., 2011; Tehrani and Ghani, 2012; Ding et al., 2010; Lavanya et al., 2012; Khatib and El., Hameed, 2011). Consequently, in present work it is intriguing to explore the structure formation and evolution of dealloying FeCoAl alloy as well as the electrochemical biosensing properties towards H_2O_2. It is interesting to find that NP-Fe_2O_3/CoO composites were straightforwardly fabricated by dealloying FeCoAl ternary alloy under free corrosion conditions at room temperature, which exhibit excellent catalytic activity toward H_2O_2 electrooxidation with a wide linear range, a lower detection limit, and a good anti-interference, showing great application potential as a H_2O_2 sensing anode catalyst.

2. Experimental

2.1. Reagents and apparatus

$Fe_5Co_5Al_{90}$ alloy foils with the thickness at 50 μm were made by refining pure Fe, Co, and Al (99.99%) in an arc-furnace, followed by melt-spinning under Ar-protected atmosphere. NP-Fe_2O_3/CoO composites were prepared by etching $Fe_5Co_5Al_{90}$ alloy foils in 2 M NaOH for 48 h at room temperature. The phosphate buffered saline (PBS, 0.1 M, pH 7.0) solution was used as detection system. H_2O_2 solution (30%) was purchased from Sinopharm Chemical Reagent Co., Ltd. Dopamine (DA), uric acid (UA), and ascorbic acid (AA) were purchased from Sigma–Aldrich. The glucose stock solution was kept overnight (at least 24 h) to allow mutarotation. All the reagents were of analytical grade, and used without further purification. Ultra-pure water (18.2 MΩ) was used in all experiments.

The morphology of the sample was characterized by a JSM-6700 field-emission scanning electron microscope (SEM) with an energy-dispersive X-ray spectrometer (EDS) for compositional analysis. Transmission electron microscopy (TEM) images were obtained through a JEM-2100 high-resolution transmission electron microscope. Powder X-ray diffraction (XRD) data was collected on a Bruker D8 advanced X-ray diffractometer using Cu KR radiation (λ=1.5418 Å) at a scan rate of 0.04° s^{-1}. Surface structure properties of the NP-Fe_2O_3/CoO composites were analyzed with ESCALab250 X-ray photoelectron spectroscopy (XPS), using a monochromatized Mg Ka X-ray as the excitation source and choosing C1 s (284.60 eV) as the reference line. All electrochemical measurements were performed using CHI 760 D electrochemical workstation (Shanghai CH Instruments Co., China).

2.2. Preparation of the modified electrodes

Catalyst ink was prepared by mixing 2.0 mg carbon powder, 3.0 mg NP-Fe_2O_3/CoO composites, 2 mL isopropanol and 400 μL nafion solutions (0.5 wt%) under sonication for 20 min. The working electrode was made by dropping 2 μL catalyst ink on a polished glassy carbon electrode (GCE, 3 mm in diameter). A conventional three-electrode cell was used with Pt foil as a counter electrode and mercury sulfate electrode as the reference electrode. All potentials presented in this study were reported with respect to the reversible hydrogen electrode (RHE).

3. Results and discussion

3.1. Characterizations

Considering that the Fe and Co are more reactive metals, the Al-based FeCoAl ternary alloy was selected as the source alloy in order to avoid the corrosion of target metals. Consequently, the main process involved alloying of the targeted transition metals with Al metal, and a selective leaching of more reactive metal in alkaline corrosion media. The component of the source alloy is around $Fe_5Co_5Al_{90}$ as analyzed by EDS (Fig. S1a, Supporting Information) which is consistent with the initial designed feeding ratio. Considering the amphoteric property of Al, NaOH solution was selected as the electrolyte to selectively dissolve Al atoms. Fig. 1a shows the typical SEM image for the resulted sample after etching FeCoAl source alloy foils in 2.0 M NaOH solution for 48 h at room temperature. It is clear that the dealloyed sample consists of a number of nanoparticles with the typical diameter around 80 nm. High magnification SEM image (Fig. 1b) shows that these nanoparticles possess nanosponge morphology with the typical pore/ligament size at 10 nm. TEM characterization (Fig. 1c) further demonstrates that the dealloyed sample has the nanoparticle nanostructure. However, the nanoporous structure is hard to discern clearly due to the overlapping of nanoporous structure among these nanoparticles. By sonicating the sample for 40 min, as shown in Fig. 1d the clear contrast between the dark skeletons and bright pores further demonstrates the formation of a three-dimensional bicontinuous network nanostructure with uniform size distributions. Such three-dimensional bicontinuous nanoporous nanostructure is beneficial for mass transport and electron conductivity during electrocatalysis (Xiao et al., 2011; Chen et al., 2007).

The bimetallic composition between Fe and Co is maintained around 1:1 (illustrated in Fig. S1b), which matches well with the initial feeding ratio in ternary source alloy. Meanwhile, the majority of Al atoms have been removed to an undetectable level, and the O element also shows higher content in the dealloyed sample, implying the formation of metal oxides. It is clear that this dealloying approach is well controllable for the resulted metal components. Considering that XPS is more sensitive to the structure properties of nanostructured metal-related nanomaterials, the electron structures of metal elements in the dealloyed sample were further examined by XPS. Fig. 2a presents the Fe 2p core levels, featuring strong Fe $2p_{1/2}$ and $2p_{3/2}$ peaks around 710.8 and 724.4 eV with weak shoulder peaks at higher binding energies of 719.0 and 733.3 eV because of the spin-orbit coupling. The satellite-like peaks are indicative of the formation of Fe_2O_3 structure (Yamashita and Hayes, 2008) with no obvious peak from metallic Fe (708 eV) observed (Saita and Maenosono, 2005), indicating that Fe_2O_3 is one of the main species in the resulted sample. The formation of Fe oxides is due to the oxidation of Fe atoms on the NP surface during the dealloying and drying procedure. The Co 2p photoemission is given in Fig. 2b, where the binding energies at 780.4 eV for $2p_{3/2}$ and 796.2 eV for $2p_{1/2}$ with the corresponding satellite structure at 786.7 and 802.5 eV can be ascribed to CoO species (Briggs and Grant, 2003). Consequently, it is clear that Fe_2O_3 and CoO co-exist in the dealloyed sample. It is conclusive that during the dealloying process Fe and Co atoms interdiffuse and grow together into nanoporous structure with the form of mixed oxides by combining with the surrounding oxygen-containing species. In our previous studies, dealloying of FeAl and CoAl alloys generates Fe_3O_4 octahedron and Co_3O_4 nanosheets, respectively (Xu et al., 2010). By comparison, it is interesting to find that the resulted morphology and oxide species are both affected due to the incorporation of Fe and Co, which attracts extremely interesting to investigate the

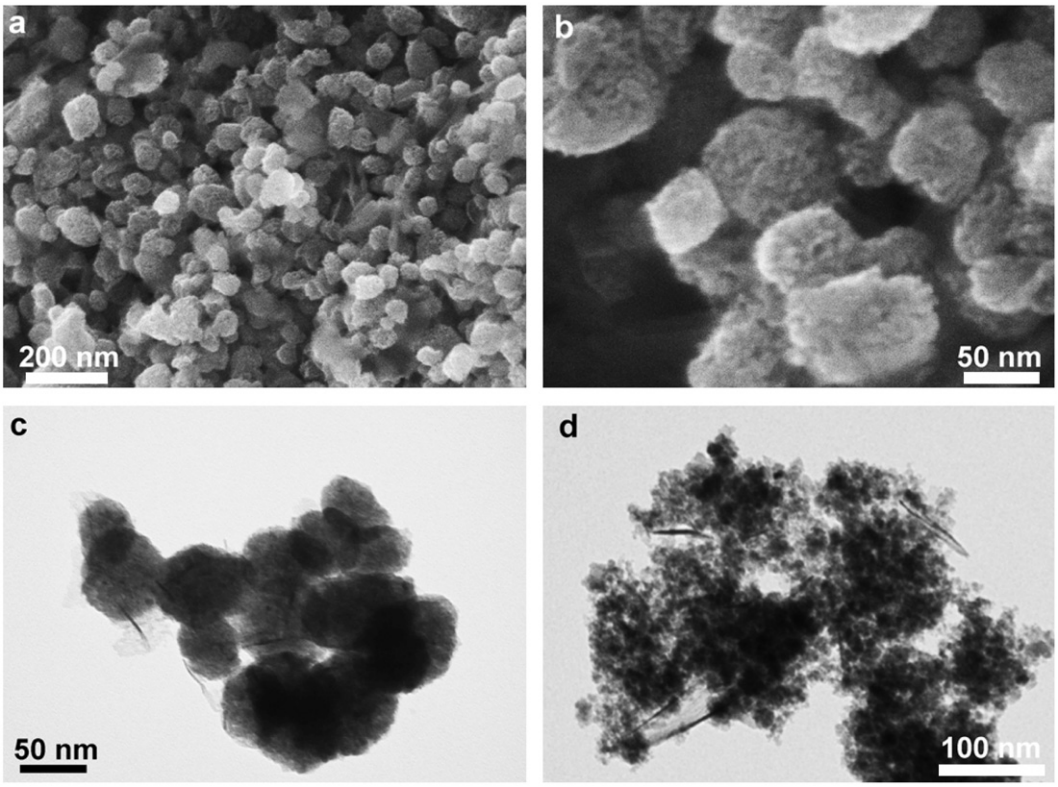

Fig.1. SEM (a and b) and TEM (c and d) images of the resulted sample upon dealloying FeCoAl alloy in 2 M NaOH solution at room temperature for 48 h.

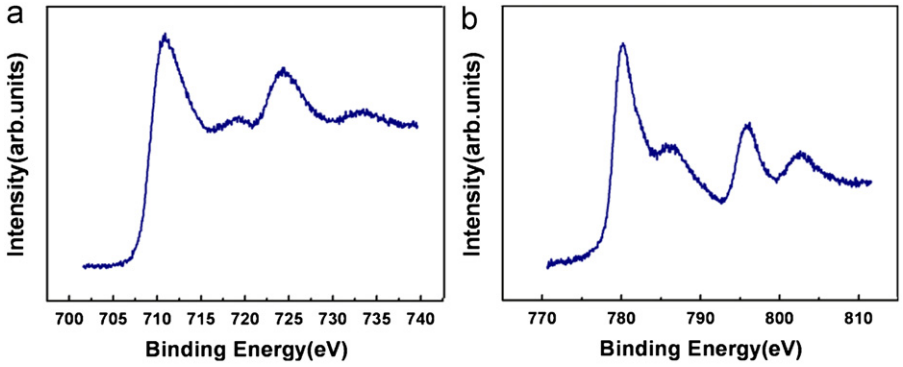

Fig. 2. XPS spectra of (a) Fe 2p and (b) Co 2p core levels for the dealloyed sample.

electrochemical properties of the composite oxides. Fig. S2 (Supporting Information) lists the diffraction patterns for the resulted metal oxide nanostructures along with Fe_2O_3 (JCPDS 39-1346) and CoO (JCPDS 42-1300) for comparison. The resulted sample shows multiple diffraction peaks as illustrated in Fig. S2. It is quite obvious that in the resulted sample there appeared five diffraction peaks at 34.5, 39.2, 56.7, 68.5, and 71.9 (2θ denoted as), which are in good agreement with the standard pattern of CoO. The additional diffraction peaks in the pattern can be ascribed to the formation of Fe_2O_3 species as compared with the standard pattern of Fe_2O_3. Therefore, the resulted sample could be determined to be the mixed oxides between Fe_2O_3 and CoO. No additional diffraction peaks related to pure Fe, Co, and Al are observed, suggesting the high purity of the resulted Fe_2O_3 and CoO composites.

The structure evolution for dealloying FeCoAl alloy was further monitored under different dealloying conditions. As shown in Fig. 3a, when FeCoAl alloy was etched in 0.5 M NaOH solution, the final sample also shows the interconnected nanosponge morphology. When the concentration of NaOH solution was increased to 5 M, nanoparticle structures generated with the typical diameter around 200 nm. In addition, it is noted that these nanoparticles are solid with no nanoporous structure observed (Fig. 3b). It is considered that at a higher NaOH concentration (such as 5 M) the etching rate becomes faster. Meanwhile, the diffusion rate of Fe and Co atoms as well the grown rate of corresponding oxides also greatly increases, consequently which leads to the formation of nanoparticle aggregates accompanied with the pore structure blocked. Based on the experimental results, it is clear that the concentration of NaOH solution has an important effect on the structure evolution of the final sample. Lower concentrations of NaOH solution are preferable for the preparation of nanoporous composite oxides with appropriate dealloying rates.

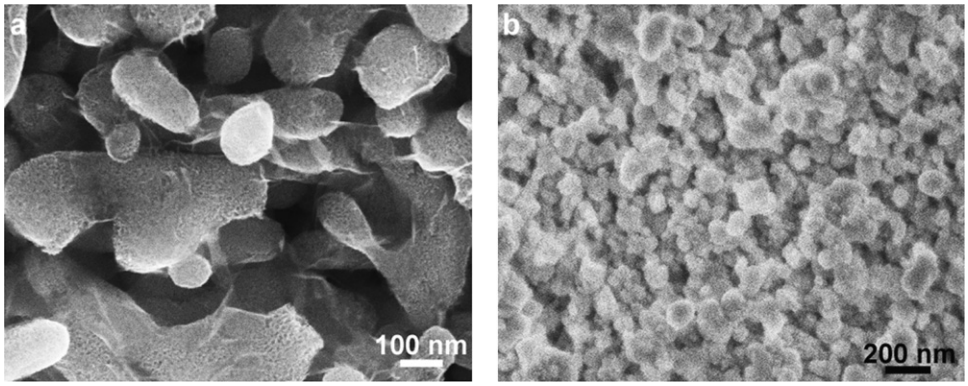

Fig.3. SEM images of the resulted samples after dealloying FeCoAl alloy in 0.5 M (a) and 5 M (b) NaOH solution at room temperature for 48 h, respectively.

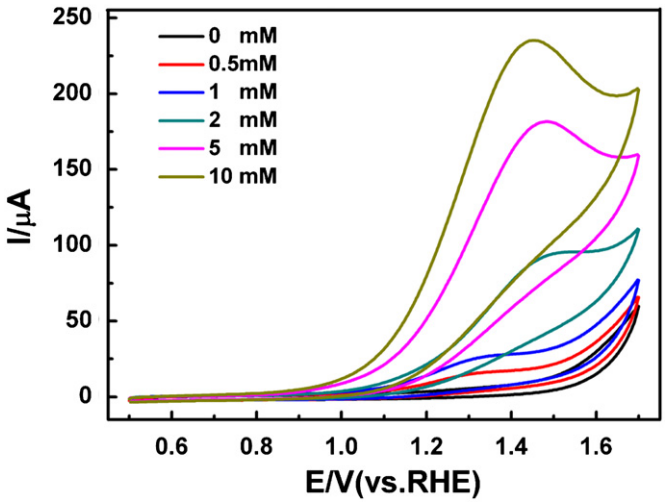

Fig. 4. CV curves of NP-Fe_2O_3/CoO composites in PBS, and PBS+H_2O_2 mixed solution with H_2O_2 concentrations of 0.5, 1, 2, 5, and 10 mM. Scan rate 50 mV/s.

3.2. Cyclic voltammetric detection of H_2O_2

Characterized by an interesting type of particularly desirable nanoporous architecture with three-dimensional bicontinuous skeleton and hollow interconnected channels extending throughout the structure, NP-Fe_2O_3/CoO composites are favorable for the unlimited transport of molecules and electron conductivity. Consequently, it is interesting to explore the electrocatalytic activity of H_2O_2 electrooxidation over the NP-Fe_2O_3/CoO composites. Fig. 4 shows the cyclic voltammetric (CV) curves of NP-Fe_2O_3/CoO composites modified electrode in 0.1 M PBS solution (pH 7.0) in the presence and absence of H_2O_2. In the blank PBS solution, there is no obvious current change beside the overpotential higher than 1.5 V. As shown in Fig. 4, an obvious oxidation peak around 1.3 V emerges in the presence of 0.5 mM H_2O_2, indicating a high catalytic activity of NP-Fe_2O_3/CoO even in the lower H_2O_2 concentration. With a further increase of H_2O_2 concentration, the oxidation current dramatically increases accompanied with the oxidation peak, meanwhile which becomes sharp and shifts to more positive potential. In addition, the onset potential for H_2O_2 oxidation shifts to lower values with an increase of H_2O_2 concentration. The obvious oxidation peak current indicates that H_2O_2 can be easily oxidized on these composite nanostructures over a broad concentration range. It implies that NP-Fe_2O_3/CoO composites have great application potential in H_2O_2 biosensing. The possible mechanism of H_2O_2 oxidation over NP-Fe_2O_3/CoO was also explored. Kafi et al. proposed that hemoglobin (Hb) immobilized in the Au films retained its bioactivity on the electrode surface. Hb (Fe^{3+}) combined with one oxygen atom of H_2O_2 to form compound ($Fe^{4+}=O$) and water. Then, the compound ($Fe^{4+}=O$) could be reduced to regenerate Hb (Fe^{3+}) (Kafi et al., 2010). H_2O_2 oxidation over NP-Fe_2O_3/CoO composites may have the similar mechanism, where one oxygen atom may combine with Fe (III) to generate water and Fe (IV)=O species. Meanwhile, the Fe (IV)=O species could be reduced to reproduce Fe (III). Similarly, Co (II) in the NP-Fe_2O_3/CoO composites catalyzes H_2O_2 by the same way.

The electrocatalytic behavior of NP-Fe_2O_3/CoO composites towards H_2O_2 oxidation was further investigated by changing the scan rate. As shown in Fig. S3a (Supporting Information), the oxidation peak currents gradually increase with increasing scan rate. As displayed in Fig. S3b, it can be observed that the anodic peak currents are linear with the scan rate in a range from 10 to 200 mV s^{-1} and the corresponding linear equations for anodic peak currents is I (μA)=0.057+1.762 υ with a linear correlation coefficient of 0.9999. These results indicate that the electrochemical oxidation of H_2O_2 on the NP-Fe_2O_3/CoO composites modified electrode is a surface-controlled process.

3.3. Electrochemical H_2O_2 biosensing

For electrochemical sensing applications, the sensing performance of electro-catalysts is usually evaluated by measuring the current response at fixed potentials versus time after the addition of analytes. Fig. 5 shows the amperometric responses of NP-Fe_2O_3/CoO composites on successive addition of H_2O_2 into the stirring PBS solution at different applied potentials. For clarity, the current responses on lower concentration of H_2O_2 solution were enlarged as shown in Fig. 5a inset. It is clear that at lower applied potential such as 1.0 V, the response current is weak to each addition of H_2O_2 from 0.05 to 0.4 mM due to lower catalytic activity of NP-Fe_2O_3/CoO composites at such potential as indicated in Fig. 4. As the applied potential is increased from 1.0 to 1.4 V, the response current to each addition of H_2O_2 gets larger. For example, at 1.3 and 1.4 V NP-Fe_2O_3/CoO composites exhibit higher current response to the addition of H_2O_2 and rapidly reach the maximum steady-state currents within 2 s. This observation is also in perfect agreement with the CV study. As shown in Fig. 5a, the NP-Fe_2O_3/CoO composites modified electrode responds rapidly and sensitively within a period of 2 s, which is much shorter than the response time on nanoporous $Pt_{46}Ni_{54}$ nanowires electrode (~5 s) (Liu et al., 2010). The fast response on NP-Fe_2O_3/CoO composites can be attributed to the fact that H_2O_2 can diffuse unlimitedly into the three-dimensional bicontinuous nanoporous structure accompanied with higher catalytic activity. As illustrated in Fig. 5b, the NP-Fe_2O_3/CoO composites exhibit excellent linear response to H_2O_2 concentration up to 4.85 mM with a lower detection limit of 0.1 μM ($S/N=3$) towards H_2O_2, which is much lower than that generated on NP-PtAg,

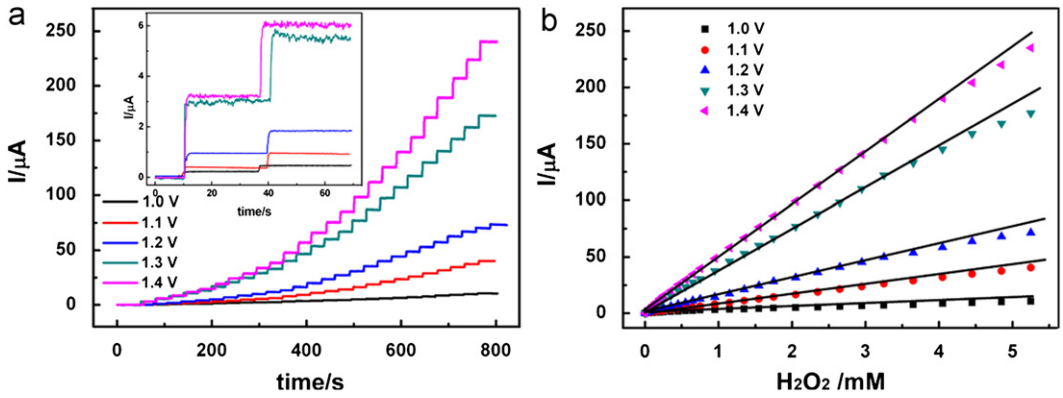

Fig. 5. (a) Amperometric current responses of NP–Fe_2O_3/CoO composites modified GCE on successive addition of H_2O_2 into stirring PBS (0.1 M, pH 7.0) at different potentials: 1.0, 1.1, 1.2, 1.3, and 1.4 V; (b) plots of current vs. H_2O_2 concentrations. Inset in a is the enlarged amperometric current responses of H_2O_2 at lower concentrations on NP-Fe_2O_3/CoO modified electrode.

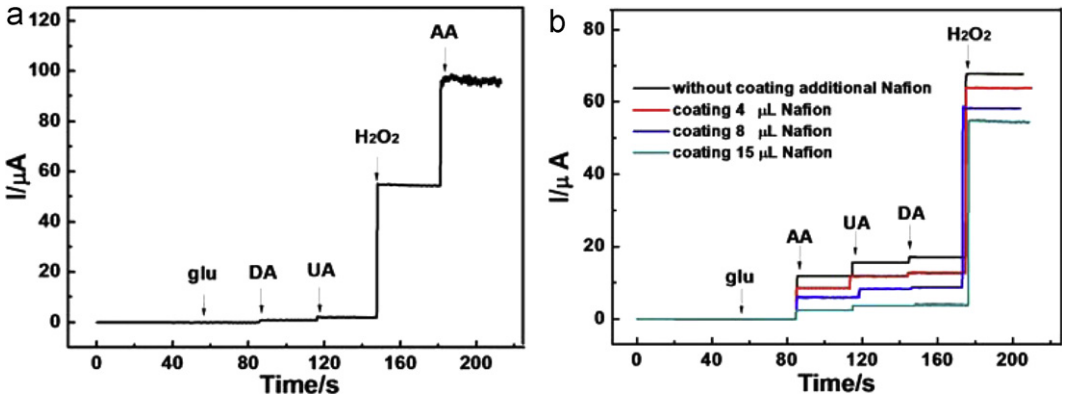

Fig. 6. (a) Amperometric responses (at 1.2 V) on NP-Fe_2O_3/CoO modified electrode by adding 5 mM glucose, 0.01 mM DA, 0.1 mM UA, 5.0 mM H_2O_2, and 0.2 mM AA in PBS solution. (b) Amperometric responses (at 1.2 V) by adding 5 mM glucose, 0.2 mM AA, 0.1 mM UA, 0.01 mM DA, and 5.0 mM H_2O_2 in PBS solution without coating additional nafion and with further coating 4, 8, and 15 μL nafion solution on NP-Fe_2O_3/CoO modified electrode.

NP-PtCu (Xu et al., 2011), and PtAu alloy nanoparticles (Safavi and Farjami, 2011). The calibration curves (Fig. 5b) indicate that the NP-Fe_2O_3/CoO composites-based biosensors have linear responses to H_2O_2 concentration in the range of 0.05–4.85 mM (at 1.1 V, linear equation: $y=0.40+7.82x$, $R=0.999$), 0.05–4.45 mM (at 1.2 V, linear equation: $y=1.21+14.53x$, $R=0.998$), 0.05–4.45 mM (at 1.3 V, linear equation: $y=3.07+35.73x$, $R=0.999$), 0.05–4.05 mM (at 1.4 V, linear equation: $y=3.61+46.39x$, $R=0.999$). A good linear range of H_2O_2 generated on the NP–Fe_2O_3/CoO composites-based biosensor is wider than that produced on NP-Au (Kafi et al., 2010), and Ni doped SnO_2 nanoparticles (Lavanya et al., 2012). The present electrode exhibits excellent sensitivity and a low detection limit compared to other electrodes based on macroporous Au-nanoparticle-doped titanium dioxide film (Wei et al., 2011), Pt nanoparticle-loaded carbon nanofiber (Liu et al., 2011), and PtPd nanoparticle decorated multi-walled carbon nanotube (Chen et al., 2012a) etc. It is concluded that the NP-Fe_2O_3/CoO composites can be used as the biosensors for H_2O_2 over a wide range of potentials. The excellent performance of NP-Fe_2O_3/CoO composites modified electrodes towards the detection of H_2O_2 makes them attractive for the fabrication of biosensor.

3.4. *The anti-interference for electrodetection of H_2O_2*

The oxidation of H_2O_2 over NP-Fe_2O_3/CoO composites locates at a relatively high potential (over 1.0 V versus RHE). At such a high potential, many other electrochemically active species that commonly co-exist in biological fluids, such as glucose, AA, UA, etc, can also be oxidized along with H_2O_2 on the electrode surface, thus generating interfering electrochemical signals to affect the detection of H_2O_2. Avoiding interference from these organic substances is a big challenge in nonenzymatic H_2O_2 detection. Thus, it is essential to investigate the anti-interference of NP–Fe_2O_3/CoO composites for H_2O_2 detection. Consequently, we selected 1.2 V as the detection potential considering the lower applied potential and the relatively large current response. For amperometric sensing applications, electrodes are generally evaluated by measuring the current response at a fixed potential and adding the analyte and possible interfering species. Herein, the anti-interference performance of NP-Fe_2O_3/CoO composites was tested by adding glucose, DA, UA, H_2O_2 and AA to PBS solution at the applied potential of 1.2 V. As illustrated in Fig. 6a, there is no response current towards glucose on NP-Fe_2O_3/CoO composites electrode and little response current to DA and UA, which can be ignored. Nevertheless, the addition of 0.2 mM AA obviously affects the response current of H_2O_2, which generates a large interfering current. The large interference from AA may originate from the accelerated oxidation after the addition of glucose, DA, UA, and H_2O_2. Wang et al. also observed the large interference of AA due to the previous addition of glucose, acetaminophen, and UA (Wang and Musameh, 2003). We further explored the anti-interference performance of NP-Fe_2O_3/CoO composites by changing the detection sequence of the interfering species with the order of adding glucose, AA, UA, DA, and H_2O_2 to PBS solution at the applied potential of 1.2 V. As illustrated in Fig. 6b, the current response on NP-Fe_2O_3/CoO for 0.2 mM AA dramatically decreased compared with Fig. 6a. In addition, we tried to continuously decrease the interference of AA by additionally dropping nafion solution as an effectively permselective barrier (Qiu et al., 2009). As shown in Fig. 6b, when 4 μL of nafion

(0.5 wt%) solution was dropped on the NP-Fe_2O_3/CoO modified electrode, there is also no response current towards glucose, and the interference current from AA is reduced. With an increase of dropped nafion solution on modified electrode surface, the interference currents from AA, UA, and DA are all gradually reduced. Importantly, the current response for H_2O_2 has almost no reduction, and all the interfering species finally exhibit much weaker signals less than 5% of the response generated by H_2O_2 on NP-Fe_2O_3/CoO modified electrode after dropping 15 μL of nafion (0.5 wt%) solution, which is acceptable in anti-interference detection. It is concluded that the as-prepared NP–Fe_2O_3/CoO composites are preferable to construct the nonenzyme biosensors towards H_2O_2 with good anti-interference performance towards glucose, DA, UA, and AA.

3.5. Long-term stability and reproducibility of the H_2O_2 biosensor

The long-term sensing stability of NP-Fe_2O_3/CoO composites electrocatalyst is essential for continuous and reliable monitoring of H_2O_2, which was evaluated by detecting the steady-state current using potentiostatic method. As displayed in Fig. S4a (Supporting Information), the addition of 0.1 mM H_2O_2 in stirring PBS solution shows a stable amperometric response after running for 2000 s with ~5% activity decay. The sensing stability of NP-Fe_2O_3/CoO composites was further explored by continuous detecting H_2O_2 every day for a period of two weeks. From Fig. S4b, the recorded amperometric response of the electrode towards 0.1 mM H_2O_2 has almost no change over a period of 14-day. These results demonstrate that NP-Fe_2O_3/CoO composites-based biosensor is highly stable and efficient at H_2O_2 detection. The high reproducibility of NP-Fe_2O_3/CoO composites modified electrodes can also be demonstrated based on the measurement results in the period of 14 days, in which the relative standard deviation (RSD) for 0.1 mM H_2O_2 is 2.61%. For three NP-Fe_2O_3/CoO composites modified electrodes, the RSD is 3.07%. It is clear that the NP-Fe_2O_3/CoO composites show good long-term stability and excellent reproducibility for H_2O_2 detection.

4. Conclusions

In summary, we reported a simple alloy corrosion route for the facile fabrication for nanostructured complex bimetallic oxides, which shows excellent electrocatalytic activity for H_2O_2 detection without any activation pretreatment. Based on the excellent electrocatalytic activity of NP-Fe_2O_3/CoO composites towards H_2O_2 oxidation in PBS solution, a sensitive nonenzymatic H_2O_2 sensor can be constructed with a wide linear range (0.05–4.85 mM) as well almost little interference from glucose, DA, UA, and AA. During the biosensing detection, NP-Fe_2O_3/CoO composites behave fast response, large oxidation current, good linear relationship toward H_2O_2 with low detection limit of 0.1 μM. Consequently, the as-made NP-Fe_2O_3/CoO composites hold great potential as a promising catalyst for H_2O_2 detection in terms of low cost, excellent catalytic performance, simple preparation, good long-term stability, and excellent reproducibility.

Acknowledgments

This work was supported by the National Science Foundation of China (Nos. 51001053, 21271085) and Shandong Province (ZR2010EQ039) and the China Postdoctoral Science Foundation (201104617).

Appendix A. Supporting information

Supplementary data associated with this article can be found in the online version at http://dx.doi.org/10.1016/j.bios.2012.11.016.

References

Bo, X.J., Bai, J., Qi, B., Guo, L.P., 2011. Biosensors and Bioelectronics 28, 77–83.
Briggs, D., Grant, J.T., 2003. Surface Analysis by Auger and X-ray Photoelectron Spectroscopy. IM Publications, Chickester, UK.
Cattarin1, S., Kramer, D., Lui, A., Musiani, M., 2009. Fuel Cells 09 (3), 209–214.
Chakraborty, S., Raj, C.R., 2009. Biosensors and Bioelectronics 24, 3264–3268.
Chen, K.J., Pillai, K.C., Rick, J., Pan, C.J., Wang, S.H., Liu, C.C., Hwang, B.J., 2012a. Biosensors and Bioelectronics 33, 120–127.
Chen, W., Cai, S., Ren, Q.Q., Wen, W., Zhao, Y.D., 2012b. Analyst 137, 49–58.
Chen, L.Y., Guo, H., Fujita, T., Hirata, A., Zhang, W., Inoue, A., Chen, M.W., 2011. Advanced Functional Materials 21, 4364–4370.
Chen, S., Li, Y., Guo, C., Wang, J., Ma, J., Liang, X., et al., 2007. Langmuir 23, 12669–12676.
Ding, Y., Wang, Y., Su, L., Bellagamba, M., Zhang, H., Lei, Y., 2010. Biosensors and Bioelectronics 26, 542–548.
Erlebacher, J., Aziz, M.J., Karma, A., Dimitrov, N., Sieradzki, K., 2001. Nature 410, 450–453.
Highfield, J., Liu, T., Loo, Y.S., Grushko, B., Borgna, A., 2009. Physical Chemistry Chemical Physics 11, 1196–1208.
Kafi, A.K.M., Ahmadalinezhad, A., Wang, J.P., Thomas, D.F., Chen, A.C., 2010. Biosensors and Bioelectronics 25, 2458–2463.
Khatib, K.M., El., Hameed, R.M.A., 2011. Biosensors and Bioelectronics 26, 3542–3548.
Koh, S., Strasser, P., 2007. Journal of the American Chemical Society 129, 12624–12625.
Kong, L., Lu, X., Bian, X., Zhang, W., Wang, C., 2010. Langmuir 26, 5985–5990.
Lavanya, N., Radhakrishnan, S., Sekar, C., 2012. Biosensors and Bioelectronics 36, 41–47.
Lai, F.J., Su, W.N., Sarma, L.S., 2010. Chemistry—A European Journal 16, 4602–4611.
Lang, X.Y., Guo, H., Chen, L.Y., Kudo, A., Yu, J.S., Zhang, W., Inoue, A., Chen, M.W., 2010. Journal of Physical Chemistry C 114, 2600–2603.
Liu, L.F., Scholz, R., Pippel, E., Gösele, U., 2010. Journal of Materials Chemistry 20, 5621–5627.
Liu, Y., Wang, D.W., Xu, L., Hou, H.Q., You, T.Y., 2011. Biosensors and Bioelectronics 26, 4585–4590.
Meng, F.H., Yan, X.L., Liu, J.G., Gu, J., Zou, Z.G., 2011. Electrochimica Ata 56, 4657–4662.
Nambiar, S.R., Prathish, K.P., Karthik, G., Rao, T.P., 2011. Biosensors and Bioelectronics 26, 3920–3926.
Niu, X.H., Chen, C., Zhao, H.L., Chai, Y., Lan, M.B., 2012. Biosensors and Bioelectronics 36, 262–266.
Qi, Z., Gong, Y.Z., Zhang, C., Xu, J.L., Wang, X.G., Zhao, C.C., et al., 2011. Journal of Materials Chemistry 21, 9716–9724.
Qiu, H.J., Xue, L.Y., Ji, G.L., Zhou, G.P., Huang, X.R., Qu, Y.B., Gao, P.J., 2009. Biosensors and Bioelectronics 24, 3014–3018.
Safavi, A., Farjami, F., 2011. Biosensors and Bioelectronics 26, 2547–2552.
Saita, S., Maenosono, S., 2005. Chemistry of Materials 17, 6624–6634.
Snyder, J., Asanithi, P., Dalton, A.B., Erlebacher, 2008. Journal of Advanced Materials 20, 4883–4886.
Tehrani, R.M.A., Ghani, S.A., 2012. Biosensors and Bioelectronics 38, 278–283.
Wang, J., Musameh, M., 2003. Analytical Chemistry 75, 2075–2079.
Wei, N.N., Xin, X., Du, J.Y., Li, J.L., 2011. Biosensors and Bioelectronics 26, 3602–3607.
Xiao, X.Y., Montaño, G.A., Edwards, T.L., Washburn, C.M., Brozik, S.M., Wheeler, D.R., 2011. Biosensors and Bioelectronics 26, 3641–3646.
Xu, C.X., Liu, Y.Q., Su, F., Liu, A.H., Qiu, H.J., 2011. Biosensors and Bioelectronics 27, 160–166.
Xu, C.X., Li, Q., Liu, Y.Q., Wang, J.P., Geng, H.R., 2012. Langmuir 28, 1886–1892.
Xu, C.X., Wang, L.Q., Wang, R.Y., Wang, K., Zhang, Y., Tian, F., et al., 2009. Advanced Materials 21, 2165–2169.
Xu, C.X., Wang, R.Y., Zhang, Y., Ding, Y., 2010. Nanoscale 2, 906–909.
Yamashita, T., Hayes, P., 2008. Applied Surface Science 254, 2441–2449.
You, M.J., Jeong, Y.N., Ahmed, M.S., Kim, S.K., Choi, H.C., Jeon, S., 2011. Biosensors and Bioelectronics 26, 2287–2291.
Yu, J.S., Ding, Y., Xu, C.X., Inoue, A., Sakurai, T., Chen, M.W., 2008. Chemistry of Materials 20, 4548–4550.